

Topological States in Finite Graphene Nanoribbons Tuned by Electric Fields

David M T Kuo

*Department of Electrical Engineering and Department of Physics,
National Central University, Chungli, 32001 Taiwan, China*

(Dated: November 12, 2024)

In this comprehensive study, we conduct a theoretical investigation into the Stark shift of topological states (TSs) in finite armchair graphene nanoribbons (AGNRs) and heterostructures under transverse electric fields. Our focus centers on the multiple end zigzag edge states of AGNRs and the interface states of 9 – 7 – 9 AGNR heterostructures. For the formal TSs, we observe a distinctive blue Stark shift in energy levels relative to the electric field within a range where the energy levels of TSs do not merge into the energy levels of bulk states. Conversely, for the latter TSs, we identify an oscillatory Stark shift in energy levels around the Fermi level. Simultaneously, we reveal the impact of the Stark effect on the transmission coefficients for both types of TSs. Notably, we uncover intriguing spectra in the multiple end zigzag edge states. In the case of finite 9 – 7 – 9 AGNR heterostructures, the spectra of transmission coefficient reveal that the coupling strength between the topological interface states can be well controlled by the transverse electric fields. The outcomes of this research not only contribute to a deeper understanding of the electronic property in graphene-based materials but also pave the way for innovations in next-generation electronic devices and quantum technologies.

I. INTRODUCTION

In the dynamic realm of nanomaterials and nanoelectronics [1-5], the investigation of unique electronic properties in graphene-based materials continues to be a focal point of scientific exploration [6-21]. Among these materials, armchair graphene nanoribbons (AGNRs) have garnered significant attention. As researchers delve into the manipulation of electronic states in nanoscale materials, an essential aspect that demands scrutiny is the Stark shift in AGNRs [22-27]. Understanding the Stark shift in AGNRs is not only crucial for tailoring the electronic properties of these materials but also for unraveling the intricate interplay between topological phases and Stark effects [24-27].

Although the Stark effects of AGNRs [22-27] and other low-dimensional materials [28– 38] have been extensively studied, it is poorly understood for Stark effect on the end zigzag edges of AGNRs [39-43] and the interfaces of AGNR heterostructures [44]. The Stark shift of these two types of topological states with localized wave functions offers new avenues for the design and optimization of nanoelectronic devices. AGNRs are envisioned as key components in future electronic circuits and transistors [29]. Moreover, the implications for optoelectronic applications cannot be understated[30], as the Stark shift in the bound states of AGNRs may influence absorption and emission properties, impacting the development of photodetectors and light-emitting diodes.

This investigation seeks to explore the Stark shift in the end zigzag edge states and topological interface states of GNRs, providing insights that could inform future developments in GNR-based quantum computing [45-47]. Our study focuses on a 13-atom-wide AGNR (13-AGNR) and a 9-7-9 AGNR heterostructure, as illustrated in Figures 1(a) and 1(b), respectively. These structures were fabricated using the bottom-up synthesis technique,

which is well-suited for producing narrow GNRs [15, 19]. Recent studies [39-43] have demonstrated long 13-AGNR segments with a degeneracy of multiple end zigzag edge states, distinct from the degeneracy observed in 7-AGNR and 9-AGNR segments. Figures 1(c) and 1(d) show the topological end zigzag edge states in a long 13-AGNR segment [39-43] and the topological states arising from the interface states of a 9-7-9 AGNR heterostructure [44]. To investigate the impact of the Stark shift on the energy levels and transport properties of these topological states, external electric fields (F_x) are applied along the zigzag edge direction (the x-direction).

We have demonstrated that the energy levels of multiple end zigzag edge states exhibit nonlinear behavior with respect to the electric field strength in a short 13-AGNR. Conversely, their response to electric fields shows linear behavior in a longer 13-AGNR. The spectra of transmission coefficients for various electric field strengths directly reveal the presence of multiple zigzag edge states. Meanwhile, the energy levels of topological interface states in the 9-7-9 AGNR segment exhibit interesting oscillatory behavior around the Fermi energy. The transmission coefficient spectra for the 9-7-9 AGNR segment indicate that the interface states are well-separated from the bulk states and electrodes. The coupling strength between these interface states can be finely adjusted by transverse electric fields. Given these characteristics, the topological interface states of AGNR heterostructures hold significant promise for the design of quantum bits [45-47].

II. CALCULATION METHODOLOGY

To investigate how external electric fields to influence charge transport through the finite GNR structure coupled to electrodes, we employ a combination of the tight-binding model and the Green's function technique

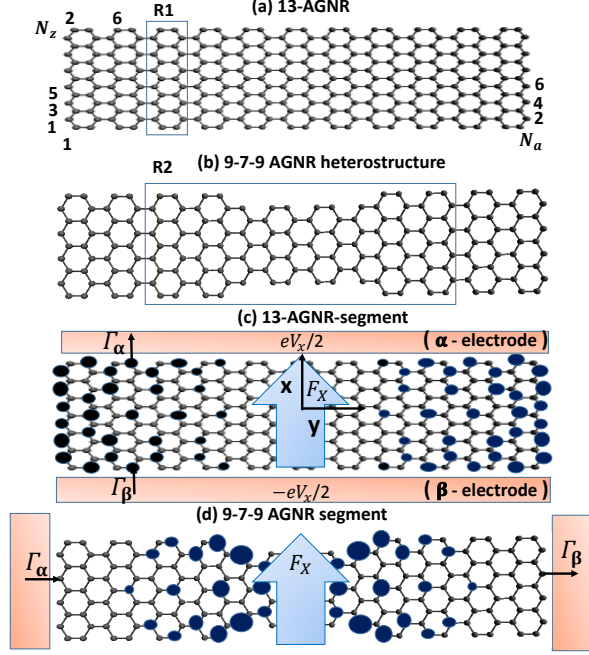


FIG. 1: (a) Schematic diagram of a 13-atom-wide armchair graphene nanoribbon (13-AGNR). (b) Structure of a 9-7-9 AGNR heterostructure. The geometries of the R_1 and R_2 unit cells are shown for the 13-AGNR and 9-7-9 AGNR heterostructure, respectively. (c) A 13-AGNR segment is connected to the α and β electrodes. The symbols Γ_α and Γ_β represent the electron tunneling rates between the α and β electrodes and the adjacent atoms at the armchair edges. (d) A 9-7-9 AGNR heterostructure segment with zigzag edges coupled to electrodes. The transverse electric field is given by $F_x = V_x/L_z$, where $L_z = \sqrt{3}a_{cc}(N_z - 1)/2$ and $a_{cc} = 1.42$, Å (carbon-carbon bond length). The x-direction is defined along the zigzag edge structure of the 13-AGNR and 9-7-9 AGNR segments. The radius of the circle represents the magnitude of the charge density for the topological states of the GNRs at $F_x = 0$.

[48,49]. The system Hamiltonian consists of two components: $H = H_0 + H_{GNR}$. In this context, H_0 signifies the Hamiltonian of the electrodes, which encompasses the interaction between the electrodes and the GNR. Meanwhile, H_{GNR} represents the Hamiltonian of GNR, which is expressed as follows:

$$H_{GNR} = \sum_{\ell,j} E_{\ell,j} d_{\ell,j}^\dagger d_{\ell,j} - \sum_{\ell,j} \sum_{\ell',j'} t_{(\ell,j),(\ell',j')} d_{\ell,j}^\dagger d_{\ell',j'} + h.c. \quad (1)$$

Here, $E_{\ell,j}$ represents the on-site energy of the orbital in the ℓ -th row and j -th column. The operators $d_{\ell,j}^\dagger$ and $d_{\ell,j}$ create and annihilate an electron at the atom site denoted by (ℓ,j) . The parameter $t_{(\ell,j),(\ell',j')}$ characterizes

the electron hopping energy from site (ℓ',j') to site (ℓ,j) . We assign the tight-binding parameters for GNR as follows: $E_{\ell,j} = E_0 + (\ell - (N_z + 1)/2)eV_x/(N_z - 1)$, where the applied voltage V_x responds to the external electric fields F_x [26]. Meanwhile, we set $t_{(\ell,j),(\ell',j')} = t_{pp\pi} = 2.7$ eV for the nearest-neighbor hopping strength. The electron hopping strengths for second- and third-neighbor interactions can be considered as a perturbative effect [40]. The calculated energy levels of the topological states, under this approximation, are in good agreement with results obtained from first-principles method (DFT) calculation [19, 42]. For simplicity, this study neglects these perturbative terms as well as electron Coulomb interactions within the topological states. However, the latter effect may induce a magnetic order parameter for the topological states in the chain [44].

The bias-dependent transmission coefficient $(\mathcal{T}_{\alpha,\beta}(\varepsilon, V_x))$ of a GNR connected to electrodes can be calculated using the formula $\mathcal{T}_{\alpha,\beta}(\varepsilon) = 4Tr[\Gamma_\alpha(\varepsilon)G^r(\varepsilon)\Gamma_\beta(\varepsilon)G^a(\varepsilon)]$ [20,21], where $\Gamma_\alpha(\varepsilon)$ and $\Gamma_\beta(\varepsilon)$ denote the tunneling rate (in energy units) at the α and β leads, respectively, and $G^r(\varepsilon)$ and $G^a(\varepsilon)$ are the retarded and advanced Green's functions of the GNRs coupled to the electrodes, respectively. The tunneling rates are determined by the imaginary part of the self-energy originating from the coupling between the α (β) electrode and its adjacent GNR atoms. In terms of tight-binding orbitals, $\Gamma_{\alpha(\beta)}(\varepsilon)$ and Green's functions are matrices. For simplicity, $\Gamma_{\alpha(\beta)}(\varepsilon)$ for interface atoms between the electrodes and the GNR possesses diagonal entries with a common value of Γ_t [48,49].

III. RESULTS AND DISCUSSION

A. Electronic Structures of AGNRs with Transverse Electric Fields

In Figures 2(a)-2(d), we present the electronic structures of 13-AGNRs shown in Fig. 1(a) for various V_x values. As depicted in Fig. 2, the application of a transverse electric field induces a transition in AGNRs from a semiconductor to a semimetal state. Several intriguing phenomena arise upon the introduction of V_x :

(a) The band gap of AGNRs ($E_g = 0.714$ eV) diminishes with increasing V_x values. Notably, when $V_x = 5.4$ V, two Fermi-Dirac cones near the Fermi level (ε_F) are observed in Fig. 2(d). This modulation of electronic structures in AGNRs by an electric field has been documented by various research groups employing different methodologies [23-26]. Furthermore, the semiconductor-to-semimetal phase transition illustrated in Fig. 2 is also applicable to AGNRs with different widths [26]. The reduction in the band gap as a function of increasing electric field for over 30 AGNRs, with widths ranging from $N_z = 11$ to $N_z = 43$, was theoretically reported in reference [26].

(b) The second derivative of the curves for the first con-

duction subband indicates that electron effective masses increase with the strength of the transverse electric field in the small field regions [23].

(c) The flat bands at $\varepsilon - \varepsilon_F = \pm 2.7$ eV for $V_x = 0$ undergo significant alterations for large $V_x \geq 1.8$ V. Analytical proofs have demonstrated the existence of flat bands in AGNRs for N_z with odd numbers [50].

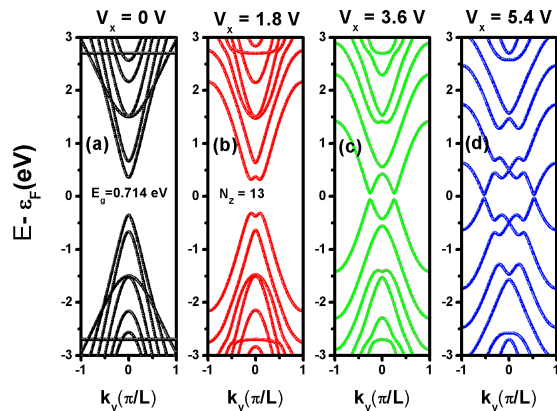


FIG. 2: Electronic subband structures for various V_x values in 13-AGNR: (a) $V_x = 0$, (b) $V_x = 1.8$ V, (c) $V_x = 3.6$ V, and (d) $V_x = 5.4$ V. Here $L = 1$ u.c.

B. Finite AGNRs with Transverse Electric Fields

In Fig. 2, the electronic states of AGNRs demonstrate the Stark effect on the bulk states. To elucidate the Stark effect on the end zigzag edge states of AGNRs, we must consider finite AGNRs. We present the calculated energy levels of finite 13-AGNRs as functions of applied voltage (V_x) for various lengths of AGNRs (N_a) in Fig. 3. For simplicity, we set $\varepsilon_F = 0$ throughout this article. In the absence of electric fields, four energy levels labeled as $\Sigma_{c,1}$, Σ_c , Σ_v , and $\Sigma_{v,1}$ exist within the energy range of $|E(\text{eV})| \leq 0.5$ eV in Fig. 3(a). The energy levels $\Sigma_{c,1}$ and Σ_c (Σ_v and $\Sigma_{v,1}$) almost merge for $N_a = 84$ ($L_a = 8.8$ nm), with a difference of $\Sigma_{c,1} - \Sigma_c = 1.72$ meV. Such behavior was also observed in previous work [41], where the author calculated the energy levels of 13-AGNRs using the DFT. In reference [41], the degeneracy of $\Sigma_{c,1}$ ($\Sigma_{v,1}$) and Σ_c (Σ_v) is referred to as multiple end zigzag edge states for large N_a values. As shown in Fig. 3(c) and 3(d), the bulk states exhibit Franz-Keldysh behavior with respect to the electric field when $V_x \geq 1.8$ V. In Fig. 3(d), it is difficult to distinguish the curve of $\Sigma_{c,1}$ ($\Sigma_{v,1}$) from Σ_c (Σ_v). These curves show a linear function of V_x before merging into the bulk states.

To further clarify the Stark effect on the energy levels of end zigzag edge states shown in Fig. 3, we present the calculated charge density distribution $|\psi(\ell, j)|^2$ of finite 13-AGNRs with $N_a = 44$ in Fig. 4. In Fig. 4(a), the charge density ($|\psi(\ell, j)|^2$) of Σ_c shows expo-

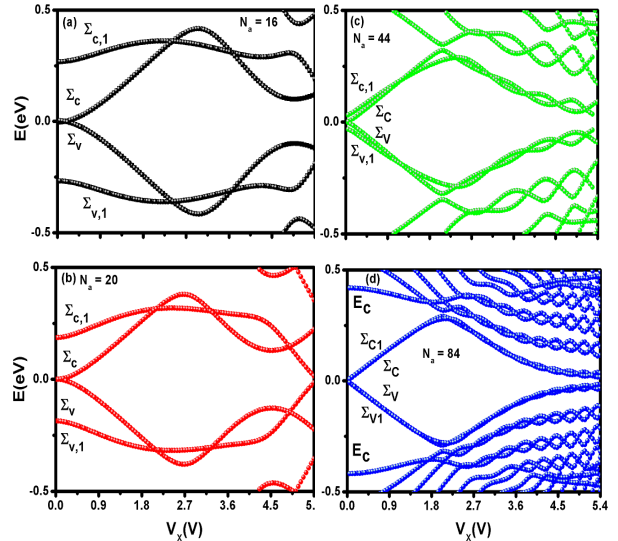


FIG. 3: Energy levels of finite 13-AGNRs as functions of applied voltage V_x for various N_a values. (a) $N_a = 16$ ($L_a = 1.56$ nm), (b) $N_a = 20$ ($L_a = 1.99$ nm), (c) $N_a = 44$ ($L_a = 4.54$ nm), and (d) $N_a = 84$ ($L_a = 8.8$ nm).

ponential decay in the armchair directions, resulting in its charge densities being most distributed at the end zigzag edge sites. Maximum charge densities appear at sites $(\ell = 6, j = 1(j = 44))$ and $(\ell = 8, j = 1(j = 44))$. As depicted in Fig. 4(b), the charge density $|\psi(\ell, j)|^2$ of $\Sigma_{c,1}$ exhibits maximum values at sites $(\ell = 4, j = 1(j = 44))$ and $(\ell = 10, j = 1(j = 44))$. The wave function of $\Sigma_{c,1}$ along the y -direction decays slower than that of Σ_c . In the presence of F_x , the charge densities of Σ_c (Σ_v) are pushed to higher (lower) potential regions in Fig. 4(c) (Fig. 4(d)), indicating that the applied electric field aligns with the dipole moment of electronic states (Σ_c and Σ_v) [51]. This explains the blue Stark shift of the end zigzag edge states (shown in Fig. 3(c) and 3(d)).

To provide more direct evidence of multiple end zigzag edge states[41], we present the calculated transmission coefficient $\mathcal{T}_{\alpha,\beta}(\varepsilon)$ of finite 13-AGNRs with $N_a = 84$ and $\Gamma_t = 0.09$ eV in Fig. 5(a)-5(f), where we consider the armchair edges of AGNRs interconnected to the electrodes as shown in Fig. 1(c). As depicted in Fig. 5(a), the quantum confinement effect of finite AGNRs enlarges the gap $E_c - E_v = 0.836$ eV, which is larger than $E_g = 0.714$ eV in infinitely long 13-AGNRs (see Fig. 2(a)). Additionally, there exists a significant peak (Σ_0) in the middle gap for $V_x = 0$. Although there are four energy levels around $\varepsilon = 0$ [42], notably the maximum $\mathcal{T}_{\alpha,\beta}(\varepsilon = 0)$ is smaller than two. To resolve these four energy levels, one must consider very weak coupling strength between the AGNRs and the electrodes (e.g.,

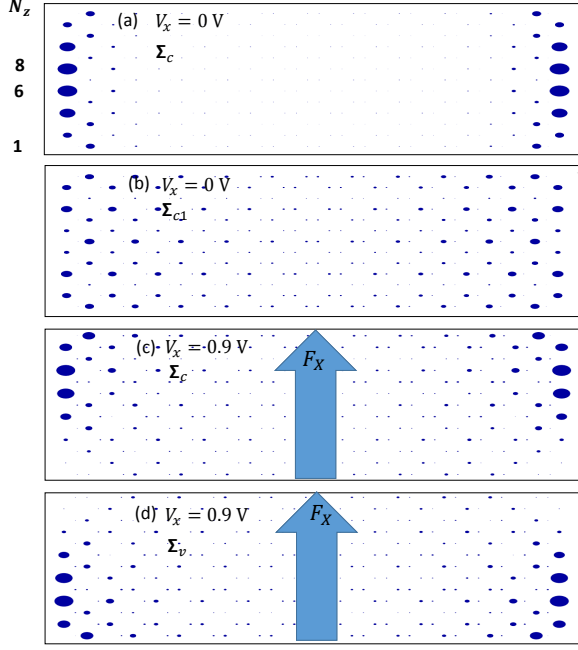


FIG. 4: Charge density ($|\Psi(\ell, j)|^2$) of 13-AGNRs with $N_a = 44$. Diagrams (a)-(d) represent the charge densities of Σ_c at $V_x = 0$, $\Sigma_{c,1}$ at $V_x = 0$, $\Sigma_c = 0.141$ eV at $V_x = 0.9$ V, and $\Sigma_v = -0.141$ eV at $V_x = 0.9$ V, respectively.

$\Gamma_t = 9$ meV). In Fig. 5(b), Σ_0 splits into ε_C and ε_V . The peaks labeled by ε_C and ε_V are larger than one. Such magnitudes of peaks larger than one are enhanced with increasing electric fields, as seen in Fig. 5(c)-5(f). The enhancement of $\varepsilon_C(V)$ larger than one is evidence of multiple end zigzag edge states of 13-AGNRs.

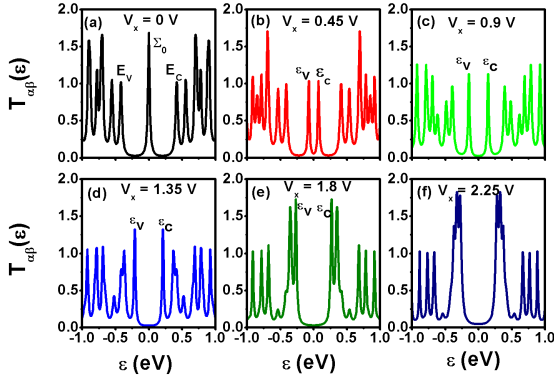


FIG. 5: Transmission coefficient $\mathcal{T}_{\alpha,\beta}(\varepsilon)$ of 13-AGNR with $N_a = 84$ and $\Gamma_t = 90$ meV for various V_x values. (a) $V_x = 0$, (b) $V_x = 0.45$ V, (c) $V_x = 0.9$ V, (d) $V_x = 1.35$ V, (e) $V_x = 1.8$ V, and (f) $V_x = 2.25$ V.

C. Electronic Structures of $9_2 - 7_3 - 9_2$ AGNR Superlattice with Transverse Electric Fields

To investigate the Stark effect on the topological states (TSs) at the interfaces between the 9-AGNR and 7-AGNR segments, we present the calculated electronic structures of $9_w - 7_x - 9_w$ AGNR superlattices (SLs) shown in Fig. 1(b) for various transverse electric fields in Fig. 6. The notations $w = 2$ and $x = 3$ denote the lengths of 9-AGNR and 7-AGNR, respectively, in units of unit cells (u.c) of AGNRs. In Fig. 6(a), we observe subbands around the Fermi energy [44], which have also been confirmed experimentally in a recent report [19]. The topological subband structures without V_x can be well described by the Su-Schrieffer-Heeger (SSH) model [52,53], which provides an analytical expression of $E(k) = \pm\sqrt{t_x^2 + t_w^2 - 2t_x t_w \cos(k(\pi/L))}$. Here, t_x and t_w represent the electron hopping strengths in the 7-AGNR segment and 9-AGNR segment, respectively, while $L = 7$ u.c denotes the length of the super unit cell [21].

In Fig. 6(a), the gap of the minibands formed by TSs is $\Delta = 76.8$ meV. This band gap exhibits oscillatory behavior with respect to V_x , as depicted in Fig. 6. Specifically, we have $\Delta = 65$ meV, $\Delta = 31.7$ meV, $\Delta = 31.7$ meV, $\Delta = 7.26$ meV, and $\Delta = 88.5$ meV for $V_x = 0.9$ V, $V_x = 1.8$ V, $V_x = 2.7$ V, $V_x = 3.6$ V, and $V_x = 4.5$ V, respectively. Even at $V_x = 4.5$ V, the topological subbands remain well separated from the bulk subbands. This unique characteristic suggests that the interface TSs can avoid noise from the bulk subbands, such as electron inter-subband transitions under optical phonon-assisted processes.

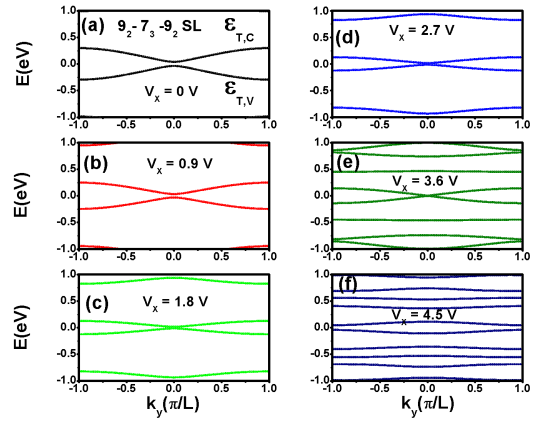


FIG. 6: Electronic structure of $9_2 - 7_3 - 9_2$ AGNR superlattice for various voltages. Diagrams (a)-(f) correspond to $V_x = 0$ V, $V_x = 0.9$ V, $V_x = 1.8$ V, $V_x = 2.7$ V, $V_x = 3.6$ V, and $V_x = 4.5$ V. Here $L = 7$ u.c.

D. $9_w - 7_x - 9_w$ AGNR Segments with Transverse Electric Fields

Although the 9-7-9 AGNR SLs fabricated using the bottom-up synthesis technique are limited in length by the 7-AGNR segment with $x = 3$ [19], we focus on the topological interface states of $9_w - 7_x - 9_w$ AGNR segments with $x = 3$ and $x = 5$ in the following discussion. In a finite $9_w - 7_3 - 9_w$ AGNR segment, the interface states represent robust topological states (TSs) resistant to defect scattering and other excitation modes due to their localized nature [19]. To elucidate the Stark shift of these TSs, we present the calculated energy levels of $9_w - 7_3 - 9_w$ AGNR segments as functions of V_x for two different lengths in Fig. 7. We consider a $9_4 - 7_3 - 9_4$ AGNR segment with $N_a = 44$ in Fig. 7(a). Four energy levels labeled by Σ_c , Σ_v , $\varepsilon_{T,C}$, and $\varepsilon_{T,V}$ are observed in the absence of an electric field. Here, $\Sigma_c = 0.18$ meV and $\Sigma_v = -0.18$ meV arise from the two end zigzag edge states, while $\varepsilon_{T,C} = 0.1167$ eV and $\varepsilon_{T,V} = -0.1167$ eV arise from the two interface states between the 9-AGNR and 7-AGNR segments [21]. These two types of TSs exhibit oscillatory Stark shift phenomena with respect to V_x . Such behaviors distinguish from the blue Stark shift of multiple end zigzag edge states of 13-AGNR shown in Fig. 3(c). To understand the Stark shift of AGNRs with different N_z from $N_z = 13$, we also calculate the end zigzag edge states of AGNR with $N_z = 9$ and $N_a = 44$ as functions of V_x (blue curve) in Fig. 7(a). This blue curve also exhibits oscillatory Stark shift.

In Fig. 7(b), we present the Stark shift of $9_8 - 7_3 - 9_8$ AGNR segment. Because the 7-AGNR segment remains as 3 unit cells, the energy levels of $\varepsilon_{T,C}$ and $\varepsilon_{T,V}$ are unchanged at $V_x = 0$. Meanwhile, $\varepsilon_{T,C}$ and $\varepsilon_{T,V}$ show a red Stark shift for V_x smaller than 2 V. To illustrate the red Stark shift phenomena, we present the charge densities of $\varepsilon_{T,C}$ and $\varepsilon_{T,V}$ at $V_x = 0.918$ V in Fig. 8. The charge density of $\varepsilon_{T,C}$ accumulates in the lower potential area, while that of $\varepsilon_{T,V}$ accumulates in the higher potential area. The electric field opposes the dipole moment of electronic states, explaining their red Stark shift at $V_x = 0.918$ V. The charge densities of $\varepsilon_{T,C}$ and $\varepsilon_{T,V}$ mainly distribute at the interfaces between 9-AGNR and 7-AGNR segments. The mixing between the end zigzag edge states and the interface states is very small when the 9-AGNR segments are enlarged. Note that in the scenario of a $9_4 - 7_3 - 9_4$ AGNR segment, the mixing between the end zigzag edge states and the interface states can be large in the presence of electric fields.

In Figs. 7(a) and (b), the length of the 7-AGNR segment remains 3 unit cells. To clarify the length effect of the 7-AGNR segment, we present the energy levels of a $9_8 - 7_5 - 9_8$ AGNR heterostructure as functions of V_x in Fig. 9. Because the length of the 7-AGNR segment is 5 unit cells, the value of t_x is reduced to -38 meV. The energy levels of $\varepsilon_{T,C(V)}$ and $\Sigma_{C(V)}$ continue to exhibit oscillatory behavior around the Fermi energy. We conclude that the oscillatory Stark shift of $\varepsilon_{T,C(V)}$ and

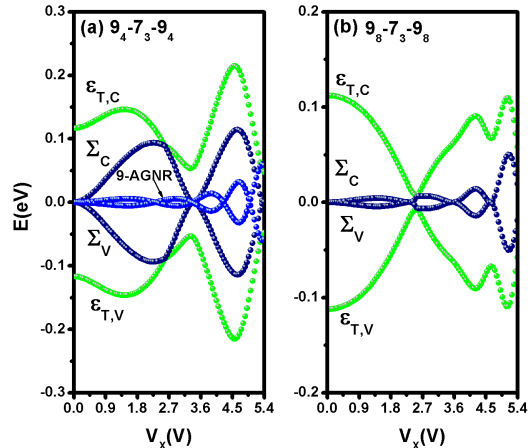


FIG. 7: Energy levels of 9-7-9 AGNR heterostructures as functions of V_x for (a) $9_4 - 7_3 - 9_4$ and (b) $9_8 - 7_3 - 9_8$.

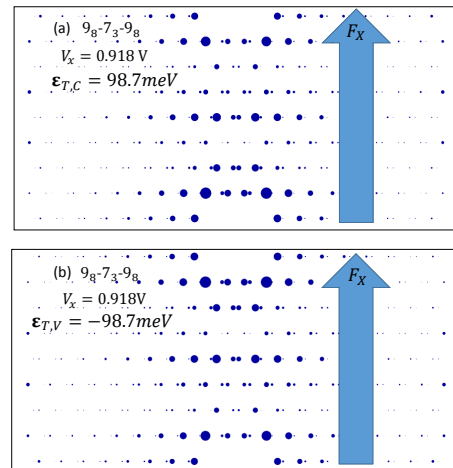


FIG. 8: Charge density ($|\psi(\ell, j)|^2$) of $9_8 - 7_3 - 9_8$ AGNR segment. (a) and (b) denote, respectively, the charge densities of $\varepsilon_{T,C} = 98.7$ meV and $\varepsilon_{T,V} = -98.7$ meV at $V_x = 0.918$ V.

$\Sigma_{C(V)}$ are essential characteristics of the TSs of 9-7-9 AGNR heterostructures.

Next, we present the transmission coefficient $\mathcal{T}_{LR}(\varepsilon)$ of $9_8 - 7_5 - 9_8$ AGNR segment with zigzag edges coupled to the electrodes as shown in Fig. 1(d). Fig. 10(a) shows the transmission coefficient for the case of $V_x = 0$. Note that in the calculation of Fig. 10, we have considered $\Gamma_t = 0.81$ eV to reveal the charge transport through the interface TSs. Because the amplitudes of charge densities for $\varepsilon_{T,C}$ and $\varepsilon_{T,V}$ are small near the end zigzag edge sites, the effective tunneling rates between the electrodes and the interface TSs are small [20]. This implies that it is difficult to reveal the spectra of $\varepsilon_{T,C}$ and $\varepsilon_{T,V}$ for small Γ_t

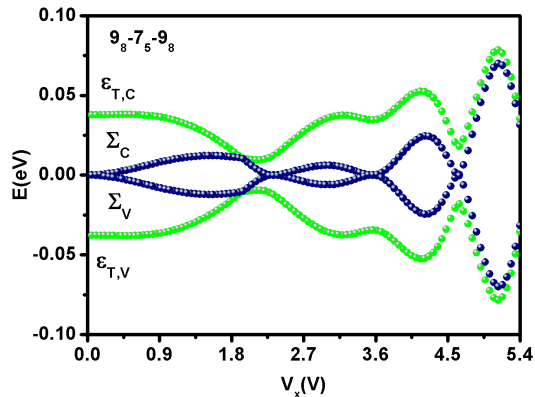


FIG. 9: Energy levels of $9_8 - 7_5 - 9_8$ AGNR segment with $L_a = 8.8$ nm as functions of V_x .

values. Although there exist the end zigzag edge states for finite $9_8 - 7_5 - 9_8$ AGNR heterostructures, charges cannot transport through such localized states for $\Gamma_t = 0.81$ eV. As depicted in Figs. 10(b)-10(f), the energy level separation $\epsilon_{T,C} - \epsilon_{T,V} = \Delta = |2t_x|$ reveals the oscillatory Stark shift phenomena of Fig. 9. The results of Fig. 10 indicate that the energy levels of TSSs resulting from the interface states between the 9-AGNR and the 7-AGNR segments can be well modulated by the transverse electric fields. Based on the results shown in Fig. 10, the topological interface states of $9_w - 7_x - 9_w$ AGNR segments effectively function as a series of double quantum dots. Therefore, they can be used to implement charge qubits designed with graphene quantum dots [45-47].

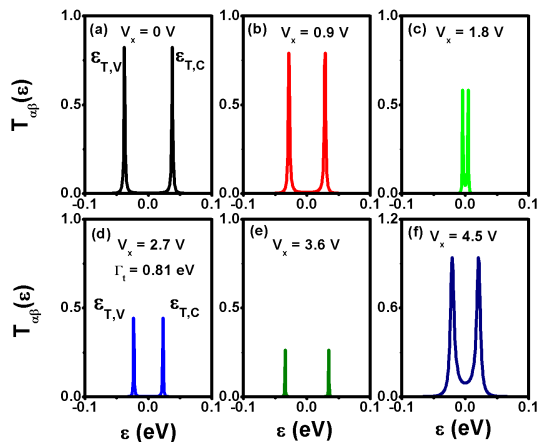


FIG. 10: Transmission coefficient $\mathcal{T}_{\alpha,\beta}(\epsilon)$ of $9_8 - 7_5 - 9_8$ AGNR segments for various electric fields at $\Gamma_t = 0.81$ eV. Diagrams (a)-(f) correspond to $V_x = 0$ V, $V_x = 0.9$ V, $V_x = 1.8$ V, $V_x = 2.7$ V, $V_x = 3.6$ V, and $V_x = 4.5$ V.

IV. CONCLUSION

We have conducted a theoretical investigation into the Stark effect on the topological states (TSSs) of finite AGNRs and heterostructures. These TSSs encompass the multiple end zigzag edge states of 13-AGNRs and the interface states of $9_w - 7_x - 9_y$ AGNR heterostructures. The multiple end zigzag edge states exhibit a blue Stark shift in their energy levels. Analysis of the charge density distribution reveals that the electric field aligns with the dipole moment of their electronic structures. In $9_w - 7_x - 9_y$ AGNR segments, both blue and red Stark shifts can occur. Specifically, in $9_4 - 7_3 - 9_4$ AGNR segments, the blue Stark shift is observed under small electric fields, while in $9_8 - 7_3 - 9_8$ AGNR segments, the red Stark shift is observed. However, these Stark shifts exhibit a common phenomenon, namely an oscillatory behavior around the Fermi energy concerning transverse electric fields.

Furthermore, we have computed the transmission coefficients ($\mathcal{T}_{\alpha,\beta}(\epsilon)$) of these two types of TSSs under transverse electric fields. The spectra of $\mathcal{T}_{\alpha,\beta}(\epsilon)$ for 13-AGNRs reveal peak magnitudes within the band gap larger than one for various transverse electric fields. This demonstration indicates that finite 13-AGNRs featuring multiple end zigzag edge states can be observed when armchair edge sites are coupled to the electrodes. Moreover, the $\mathcal{T}_{\alpha,\beta}(\epsilon)$ of $9_8 - 7_5 - 9_8$ AGNR segments illustrates that the topological interface states between the 9-AGNR and the 7-AGNR segments can be effectively modulated by transverse electric fields. Such characteristics hold significant promise for employing these TSSs as charge qubits[45,46].

Data availability statement All data that support the findings of this study are included within the article (and any supplementary files.)

Acknowledgments

This work was supported by the National Science and Technology Council, Taiwan under Contract No. MOST 107-2112-M-008-023MY2.

E-mail address: mtkuo@ee.ncu.edu.tw

- ¹ Castro N, Guinea F, Peres N M R, Novoselov K S, and Geim A K, *Reviews of Modern Physics* **81**, 109-162 (2009).
- ² Avouris P, Chen Z H, and Perebeinos V, *Nature Nanotechnology* **2**, 605 (2007).
- ³ Schwierz F, *Nature Nanotechnology* **5**, 487 (2010).
- ⁴ Radisavljevic B, Radenovic A, Brivio J, Giacometti V, and Kis A, *Nature Nanotechnology* **6**, 147 (2011).
- ⁵ Cahangirov S, Topsakal M, Akt K E, Sahin H, and Ciraci S, *Phys. Rev. Lett.* **102** 6804 (2009).
- ⁶ Son Y W, Cohen M L, and Louie S G, *Phys. Rev. Lett.* **97**, 6803 (2006).
- ⁷ Son Y W, Cohen M L, and Louie S G, *Nature* **444**, 347 (2006).
- ⁸ Jia X T et al, *Science* **323**, 1701 (2009).
- ⁹ Cai J, Ruffieux P, Jaafar R, Bieri M, Braun T, Blankenburg S, Muoth M, Seitsonen A P, Saleh M, Feng X, Mullen K and Fasel R, *Nature* **466**, 470 (2010).
- ¹⁰ Magda G Z, Jin X Z, Hagymai I, Vancso P, Osvath Z, Nemes-Incze P, Hwang C Y, Biro L P, and Tapaszt L, *Nature* **514**, 608 (2014).
- ¹¹ Ruffieux P, Wang S Y, Yang B, Sanchez-anchez C, Liu J, Dienel T, Talirz L, Shinde P, Pignedoli C A, and Passerone D, *Nature* **531**, 489 (2016).
- ¹² Liu J Z, Li B W, Tan Y Z, Giannakopoulos A, Sanchez-Sanchez C, Beljonne D, Ruffieux P., Fasel R, Feng X L, and Mullen K, *J. Am. Chem. Soc.* **137**, 6097 (2015).
- ¹³ Lee L Y, Zhao F Z, Cao T, Jisoon I and Louie S G *Nano Lett.* **18** 7274 (2018).
- ¹⁴ Arnold F M, Liu T J, Kuc A, and Heine T, *Phys. Rev. Lett.* **129**, 216401 (2022).
- ¹⁵ Llinas J P, Fairbrother A, Borin Barin G, Shi W, Lee K, Wu S, Choi B Y, Braganza R, Lear J, and Kau N, *Nat. Commun.*, **8**, 633 (2017).
- ¹⁶ Chen Y C, Cao T, Chen C, Pedramraz Z, Haberer D, de Oteyza D G, Fischer R, Louie S G, and Crommie M F, *Nat. Nanotechnol.* **10**, 156 (2015).
- ¹⁷ Rizzo D J, Veber G, Jiang J W, McCurdy R, Bronner T, Cao T, Chen T, Louie S G, Fischer F R and Crommie M F, *Science* **369**, 1597 (2020).
- ¹⁸ Sun Q, Yan Y, Yao X L, Mullen K, Narita A, Fasel R and Ruffieux P, *J. Phys. Chem. Lett.* **12**, 8679 (2021).
- ¹⁹ Rizzo D J, Jiang J W, Joshi D, Veber G, Bronner C, Durr R A, Jacobse P H, Cao T, Kalayjian A, Rodriguez H, Butler P, Chen T, Louie S G, Fischer F R and Crommie M F, *ACS Nano* **15**, 20633 (2021).
- ²⁰ Kuo D M T, *Nanomaterials* **13**, 1757 (2023).
- ²¹ Kuo D M T, *Nanotechnology* **34**, 505401 (2023).
- ²² Novikov D S, *Phys. Rev. Lett.* **99**, 056802 (2007).
- ²³ Hassan R and Kan E C, *Phys. Rev. B* **77**, 085408 (2008).
- ²⁴ Zhao F Z, Cao T and Louie S G, *Phys. Rev. Lett.* **127**, 166401 (2021).
- ²⁵ Wang X, Cui Y Q, Zhang L, and Yang M L, *Nano Research*, **14**, 3935 (2021).
- ²⁶ Pizzochero M, Tepliakov N V, Mostofi A A and Kaxiras E, *Nano Lett.* **21**, 9332 (2021).
- ²⁷ Tepliakov N V, Ma R, Lischner J, Kaxiras E, Mostofi A A, and Pizzochero M, *Nano Lett.* **23**, 6698 (2023).
- ²⁸ Okeeffe J, Wei C, and Cho K, *Appl. Phys. Lett.* **80**, 676 (2002).
- ²⁹ Bennett P B, Pedramrazi Z, Madani A, Chen Y C, de Oteyza Dimas G, Chen C, Fischer F R, Crommie M F, and Bokor J, *Appl. Rev. Lett.* **103**, 253114 (2013).
- ³⁰ Chang C P, Huang Y C, Lu C L, Ho J H, Li T S, and Lin M F, *Carbon* **44**, 508 (2006).
- ³¹ Park C H and Louie S G, *Nano Letters*, **8**, 2200 (2008).
- ³² Zhang Z H and Guo W, *Phys. Rev. B* **77**, 075403 (2008).
- ³³ Tran V T, Saint-Martin J, and Dollfus P, *Appl. Phys. Lett.* **105**, 073114 (2014).
- ³⁴ Wu Q Y, Shen L, Yang M, Cai Y Q, Huang Z G and Feng Y P, *Phys. Rev. B* **92**, 035436 (2015).
- ³⁵ Pedersen T G, *Phys. Rev. B* **96**, 115432 (2017).
- ³⁶ Zamani S and Farghadan R, *Phys. Rev. B* **99**, 235418 (2019).
- ³⁷ Wei Y D, Li W, Jiang Y Y, and Cheng J L, *Phys. Rev. B* **104**, 115402 (2021).
- ³⁸ Kuo D M T, *Phys. Chem. Chem. Phys.*, **26**, 27591 (2024).
- ³⁹ Zdetsis A D, *J. Phys. Chem. A* **124**, 976-986 (2020).
- ⁴⁰ Lopez-Sancho M P and Carmen Munoz M, *Phys. Rev. B*, **104**, 245402 (2021).
- ⁴¹ Zdetsis A D, *Carbon* **199**, 329 (2022).
- ⁴² Zdetsis A D, *Carbon* **210**, 118042 (2023).
- ⁴³ Kuo D M T, *RSC Adv.* **14**, 20113 (2024).
- ⁴⁴ Cao T, Zhao F Z, and Louie S G, *Phys. Rev. Lett.* **119**, 076401 (2017).
- ⁴⁵ Chen C C and Chang Y C, *Phys. Rev. B* **92**, 245406 (2015).
- ⁴⁶ Trauzettel B, Bulaev D V, Loss D, and Burkard G, *Nat. Phys.* **3**, 192 (2007).
- ⁴⁷ Bockrath M, *Nano Lett.* **20**, 2937-938 (2020).
- ⁴⁸ Kuo D M T and Chang Y C, *Nanomaterials* **12**, 3357 (2022).
- ⁴⁹ Kuo D M T, *RSC Adv.*, **14**, 3513 (2024).
- ⁵⁰ Zheng H X, Wang Z F, Luo T, Shi Q W, and Chen J, *Phys Rev. B* **75**, 165414 (2007).
- ⁵¹ Li D H, Zhang J, Zhang Q, and Xiong Q H, *Nano Lettes* **12**, 2993 (2012).
- ⁵² Su W P, Schrieffer J R and Heeger A J, *Phy. Rev. B* **22**, 2099 (1980).
- ⁵³ Obana D, Liu F and Wakabayashi K, *Phys Rev. B* **100**, 075437 (2019).